The Astrophysical Journal Supplement Series, 271:35 (17pp), 2024 March https://doi.org/10.3847/1538-4365/ad20c9
© 2024. The Author(s). Published by the American Astronomical Society.
OPEN ACCESS

The EDGE-CALIFA Survey: An Extragalactic Database for Galaxy Evolution Studies

Tony Wong[1], Yixian Cao[1,2], Yufeng Luo[3], Alberto D. Bolatto[4], Sebastián F. Sánchez[5], Jorge K. Barrera-Ballesteros[5], Leo Blitz[6], Dario Colombo[7], Helmut Dannerbauer[8,9], Alex Green[1], Veselina Kalinova[7], Ferzem Khan[1], Andrew Kim[1], Eduardo A. D. Lacerda[5], Adam K. Leroy[10], Rebecca C. Levy[4,11,15], Xincheng Lin[1], Yuanze Luo[1,12], Erik W. Rosolowsky[13], Mónica Rubio[14], Peter Teuben[4], Dyas Utomo[10], Vicente Villanueva[4], Stuart N. Vogel[4], and Xinyu Wang[1]

[1] Department of Astronomy, University of Illinois, Urbana, IL 61801, USA; wongt@illinois.edu
[2] Max-Planck-Institut für extraterrestrische Physik, Giessenbachstraße 1, D-85748 Garching, Germany
[3] Department of Physics and Astronomy, University of Wyoming, Laramie, WY 82071, USA
[4] Department of Astronomy, University of Maryland, College Park, MD 20742, USA
[5] Instituto de Astronomía, Universidad Nacional Autónoma de México, A.P. 70-264, 04510 México, D.F., Mexico
[6] Department of Astronomy, University of California, Berkeley, CA 94720, USA
[7] Max-Planck-Institut für Radioastronomie, D-53121, Bonn, Germany
[8] Instituto de Astrofísica de Canarias, E-38205 La Laguna, Tenerife, Spain
[9] Universidad de La Laguna, Dpto. Astrofísica, E-38206 La Laguna, Tenerife, Spain
[10] Department of Astronomy, The Ohio State University, Columbus, OH 43210, USA
[11] Steward Observatory, University of Arizona, Tucson, AZ 85721, USA
[12] William H. Miller III Department of Physics and Astronomy, Johns Hopkins University, Baltimore, MD 21218, USA
[13] Department of Physics, University of Alberta, Edmonton, T6G 2E1, Canada
[14] Departamento de Astronomía, Universidad de Chile, Casilla 36-D, Santiago, Chile
Received 2023 September 21; revised 2024 January 10; accepted 2024 January 19; published 2024 March 7

Abstract

The EDGE-CALIFA survey provides spatially resolved optical integral-field unit and CO spectroscopy for 125 galaxies selected from the Calar Alto Legacy Integral Field Area Survey (CALIFA) Data Release 3 sample. The Extragalactic Database for Galaxy Evolution (EDGE) presents the spatially resolved products of the survey as pixel tables that reduce the oversampling in the original images and facilitate comparison of pixels from different images. By joining these pixel tables to lower-dimensional tables that provide radial profiles, integrated spectra, or global properties, it is possible to investigate the dependence of local conditions on large-scale properties. The database is freely accessible and has been utilized in several publications. We illustrate the use of this database and highlight the effects of CO upper limits on the inferred slopes of the local scaling relations between the stellar mass, star formation rate (SFR), and H_2 surface densities. We find that the correlation between H_2 and SFR surface density is the tightest among the three relations.

Unified Astronomy Thesaurus concepts: Molecular gas (1073); Star formation (1569); Astronomy databases (83); Galaxy evolution (594); Spiral galaxies (1560)

1. Introduction

Over the past two decades, observational surveys have established a number of key scaling relations among galaxy properties. Of primary importance is the correlation between a galaxy's star formation rate (SFR) and its stellar mass (M_*), which for star-forming galaxies follows a tight relationship known as the star-forming "main sequence" (SFMS; Brinchmann et al. 2004; Salim et al. 2007). The SFR in turn is expected to be closely linked to the supply of star-forming gas, a quantity that is traditionally probed with radio observations of H I and CO emission, tracing the atomic and molecular gas respectively. At the same time, studies that combine SFR and gas measurements have been critical to understanding the cycling of gas in galaxies, and form the basis of another important scaling relation, the "star formation law," linking the SFR with gas content (Kennicutt & Evans 2012). Studies of the integrated gas content of galaxies, e.g., xCOLD GASS (Saintonge et al. 2017), have established that the molecular gas mass M_{H_2} is the main determinant of a galaxy's offset in SFR relative to the main sequence (Saintonge & Catinella 2022). Thus, for main-sequence galaxies, all three of the quantities M_{H_2}, M_*, and SFR are tightly correlated. Spatially resolved studies of main-sequence galaxies, although limited to smaller samples, have established that these correlations are also observed among the mass surface densities of H_2, stars, and SFR within galaxies (Wong & Blitz 2002; Bigiel et al. 2008; Wong et al. 2013; Cano-Díaz et al. 2016; Lin et al. 2019).

The Extragalactic Database for Galaxy Evolution (EDGE) survey (Bolatto et al. 2017) was the first galaxy survey to couple CO interferometry, from the Combined Array for Research in Millimeter-wave Astronomy (CARMA), with a large optical program of integral-field spectroscopy, the Calar Alto Legacy Integral Field Area Survey (CALIFA; Sánchez et al. 2016a). CALIFA provides a full suite of spatially resolved spectroscopic indicators for abundances, ionization, extinction-corrected SFR, stellar population ages, star formation histories, and kinematics (Sánchez et al. 2016b) for a well-defined sample that is designed to be representative of the $z = 0$ Universe (Sánchez et al. 2012). EDGE provides the key molecular gas information for a subsample of infrared-selected

[15] NSF Astronomy and Astrophysics Postdoctoral Fellow.

Original content from this work may be used under the terms of the Creative Commons Attribution 4.0 licence. Any further distribution of this work must maintain attribution to the author(s) and the title of the work, journal citation and DOI.

CALIFA galaxies. Here, we briefly summarize some of the main scientific highlights of EDGE. Globally, and consistent with previous work (Saintonge et al. 2011), the EDGE-CALIFA galaxies show a positive correlation between the molecular gas depletion time ($\tau_{\rm dep,mol}$) and M_* (Bolatto et al. 2017), implying that more massive galaxies are less efficient at turning their observed molecular gas into stars. On resolved ($\sim$1–2 kpc) scales, the depletion time is also longer in early-type and massive galaxies (Bolatto et al. 2017; Colombo et al. 2018; Villanueva et al. 2021), but shows no clear relationship with stellar mass surface density (Σ_*) or the Toomre Q instability parameter for stars and gas, and indeed, both the increases and decreases in $\tau_{\rm dep,mol}$ with radius are observed (Utomo et al. 2017). These results underscore the influence of both local and global galaxy properties for the star formation efficiency. The EDGE-CALIFA data also enable detailed studies of CO kinematics, which have been used to validate common approaches to deriving the circular velocity from stellar kinematics (Leung et al. 2018), and demonstrate the influence of thick ionized gas disks on Hα rotation curves (Levy et al. 2018, 2019). More recently, the EDGE-CALIFA collaboration has obtained additional CO observations of CALIFA galaxies with the Atacama Pathfinder Experiment (APEX) and the Atacama Compact Array (ACA), in Colombo et al. (2020), Sánchez et al. (2021), Garay-Solis et al. (2023), and Villanueva et al. (2024), but these data sets are not discussed in the present paper.

The need to efficiently manage both spatially resolved and global quantities spurred the design and development of a custom database for use within the EDGE collaboration. The key requirement was to provide, for each galaxy in the sample, a set of global values, 1D profiles, and 2D images, in separate tables that were easily joined for analysis. Over the course of the EDGE project, a number of intermediate databases have been generated, the most important being the structured query language (SQL) database used in Bolatto et al. (2017), Dey et al. (2019), and Cao et al. (2023). While SQL is a powerful and well-established database query language, the modest size of the EDGE repository led us to ultimately adopt a simpler approach based on Astropy tables (Astropy Collaboration et al. 2013, 2018, 2022). A pure Python implementation simplifies both the generation of and interaction with the database. The Python-based EDGE-CALIFA database (`edge_pydb`) presented in this paper is the successor to the SQL database, retaining essentially the same information aside from the use of a square rather than hexagonal sampling grid and important differences in handling of the CALIFA data described in Section 4. Preliminary versions of the Python-based database have been used to produce results presented in Barrera-Ballesteros et al. (2021), Sánchez et al. (2021), Villanueva et al. (2021), and Ellison et al. (2021). An important aspect of our approach is that the format of the tables is largely secondary; we have found the enhanced character separated values (ECSV) format suitable for the global and 1D profiles and the hierarchical data format version 5 (HDF5) format suitable for 2D images, but any format that supports preservation of metadata (including FITS) would also suffice. While HDF5 offers improvements relative to FITS in terms of input/output speed and compression, this is of secondary importance for our purposes compared to offering a clear distinction between the original image data and the derived data tables.

In this paper, we provide a detailed description of the construction of the database (Section 2), discuss some scientific applications (Section 3), and provide a comparison with the previous-generation EDGE database (Section 4). We summarize our results in Section 5.

2. Database Construction

2.1. Input Data Products

Bolatto et al. (2017) presented the original EDGE-CALIFA sample (hereafter simply the "EDGE sample"), consisting of 126 galaxies from Data Release 3 (DR3) of the CALIFA integral field unit (IFU) survey (Sánchez et al. 2016a) that were observed in CO and ^{13}CO by CARMA. To briefly summarize, the CALIFA main sample of 667 galaxies was randomly selected for observation from a 937 galaxy "mother sample" derived from diameter (r-band isophotal major axis between 45″ and 80″) and redshift ($0.005 < z < 0.03$) cuts applied to the seventh data release (DR7; Abazajian et al. 2009) of the Sloan Digital Sky Survey (SDSS). The EDGE subsample was additionally selected to have high infrared flux (as measured by the Wide-field Infrared Survey Explorer, hereafter WISE, 22 μm survey, Wright et al. 2010), and a possible CO detection in CARMA's E configuration (used to initially survey 177 galaxies) was a prerequisite for continuing with CARMA observations in the D configuration. As a result, the EDGE galaxies tend to have higher gas content and star formation activity compared to the overall CALIFA main sample. More details about the EDGE sample and the CARMA observations are provided in Bolatto et al. (2017).

For each galaxy, we obtain three data cubes, an optical cube covering 4200–7100 Å (unvignetted) with a channel width of 2 Å and an FWHM resolution of 6 Å (CALIFA *V500* setup), and CO and ^{13}CO cubes covering a typical velocity range of 860 km s^{-1} (centered on the galaxy's systemic velocity) with a channel spacing of 20 km s^{-1} derived from downsampling the original 3.4 km s^{-1} (CO) and 14.3 (^{13}CO) km s^{-1} spectral channels. The field of view for CARMA EDGE extends to offsets of $\sim$50″ (50% sensitivity contour) while the hexagonal field of view for CALIFA extends to $\sim$35″. CALIFA data for one galaxy, NGC 2486, were excluded from DR3 due to poor quality, and the corresponding CARMA data show only a marginal detection of CO. We therefore drop this galaxy from the final database, leaving a sample of 125 galaxies. The ^{13}CO cubes have much lower signal-to-noise (owing to the faintness of the line) and are analyzed in a separate paper (Cao et al. 2023). While we focus on the optical and CO data in this paper, similar data products are available for ^{13}CO.

We note that the native spectral resolution of the CO data is $\sim$5 km s^{-1}, and that the EDGE collaboration has also generated cubes with 10 km s^{-1} channel spacing. These have been used for particular applications where the velocity resolution is critical (e.g., studies of CO kinematics), but for most applications, a 20 km s^{-1} channel spacing is preferred because of improved sensitivity per channel. The `edge_pydb` database is therefore based on cubes that employ a 20 km s^{-1} channel spacing. Similarly, higher spectral resolution CALIFA products are also available using the *V1200* spectral setup, but these are over a more limited velocity range (excluding the important Hα line), so these are not included in the general-purpose database.

While the CO cubes have a typical synthesized beam FWHM of 4.″5 (Bolatto et al. 2017), given the ellipticity of the

beams, we convolve to a common 7″ curcular beam to produce the database. At this resolution, the typical 3σ sensitivity limit of the CO data is 3 K km s^{-1}, corresponding to 13 $M_\odot$ pc^{-2} of molecular gas. Matching to 7″ resolution requires degrading the CALIFA images from their native resolution of approximately 2.″5 (FWHM), so we also construct a CALIFA-only database at the native resolution, as discussed further below.

2.2. Overall Database Architecture

In constructing a database for legacy reuse, it became clear that the data can span a dimensionality from 0 (single value for a whole galaxy) to 3 (values that depend on sky position and radial velocity). To minimize redundancy, it is best to store the data in its lowest dimensional form, and replicate it along additional axes only as needed. Given our modest sample size, we found that the tables of dimensionality 0 and 1 could effectively be stored as plain text, in the self-documenting ECSV format. For the EDGE sample, a 0D table contains only ∼100 rows, and a 1D table (e.g., radial profiles, rotation curves, or integrated spectra) will increase the number of rows by a factor of 10–40, which is still manageable in textual format. Higher dimensional tables are stored in a binary compressed format (HDF5).

Even for data of the same dimensionality, it can be advantageous to create separate data tables, corresponding to different data sets or analyses, which may be updated over time. For example, a table of global photometric parameters from SDSS can be maintained separately from similar parameters derived from CALIFA or the NASA Extragalactic Database (NED). Alternatively, one may wish to create separate versions of a table corresponding to different resolutions of the same data, or different ways of masking a spectral data cube. Tables can then be joined as needed to avoid handling unnecessarily large tables. To facilitating the joining process, we use standard names for the index columns that are used to match different tables, and we try to avoid duplication of column names for tables that are likely to be joined.

Finally, in addition to the tables themselves, we have created a Python `EdgeTable` class, which is a subclass of the `astropy.table.Table` class. This allows an experienced Python user to immediately get to work joining and plotting the tables. We have added some basic plotting capabilities that are demonstrated in a set of accompanying Jupyter notebooks. The class is made available through the Python package `edge_pydb`,[16] which can be installed via the standard Python Package Index (PyPI) package manager (using the `pip` command). The package includes the full Python source code needed to regenerate the database from FITS images.

We discuss the components of the database in further detail below. We first describe the global parameter (0D) tables, followed by the 2D and 3D image tables, and finally the 1D profiles (which are generally based on analysis of the higher dimensional data).

2.3. Global Parameter Tables

The global parameter tables are organized into four groups, as described below.

Characteristics of radio observations. These include the characteristics of the CO data such as the beam size, integration time, channel noise, systemic velocity adopted for the observation, and integrated line fluxes for H I, CO, and ^{13}CO emission. H I fluxes in units of Jy km s^{-1} are derived from spectra obtained in the Green Bank Telescope (GBT) program 15B-287 (PI: D. Utomo) and from archival spectra published by van Driel et al. (2001), Springob et al. (2005), and Masters et al. (2014). Details about the GBT observations will be presented in D. Wen et al. (2024, in preparation). CO and ^{13}CO fluxes are provided in the same units and are measured from cubes at both the native resolution (`edge_coflux_natv.csv`) and a common resolution of 7″ (`edge_coflux_smo7.csv`). Multiple CO tables with similar file names (e.g., `edge_coobs_D.csv`, `edge_coobs_E.csv`, and `edge_coobs_DE.csv`) are present because CARMA observations were conducted in the E configuration for 177 galaxies and in the D configuration for 126 galaxies, yielding a set of low-resolution cubes derived from E array data only, in addition to the principal set containing both D and E array data. Furthermore, the D+E cubes were generated at two velocity resolutions (10 and 20 km s^{-1}) and at two angular resolutions (native elliptical beam and a common 7″ circular beam). While characteristics of these different cubes are provided in separate ECSV files or table columns, the user should note that only the combined (D+E) products with a 7″ beam and 20 km s^{-1} channels are provided as 2D and 3D image tables.

External databases. These tables collect galaxy properties summarized in the LEDA[17] (Makarov et al. 2014) and NED[18] databases, including coordinates, morphology, orientation parameters, diameter, redshift, and distance. Tables of WISE photometry from Bitsakis et al. (2019), corrected following the discussion in Levy et al. (2019, their Section 5.2), and the Galactic extinction from Schlegel et al. (1998) are also provided.

The LEDA table is of particular importance because it provides the primary source for the coordinates of the galaxy centers, as well as the major axis position angles and inclinations, the latter derived from the apparent axis ratio using Equations (1) and (2) from Bottinelli et al. (1983). These orientation parameters are used to determine the galactocentric polar coordinates that are provided in the 2D table (e.g., Table 2). A Python function (`edge_pydb.conversion.gc_polr`) is provided to recalculate these coordinates based on different assumed orientation parameters.

CALIFA parameters. These include galaxy properties derived from analyses conducted by the CALIFA consortium. Examples include global measures of extinction, SFR, and stellar mass, effective radii from SDSS photometry, age and metallicity obtained from the `Pipe3D` analysis pipeline (Sánchez et al. 2016b), distances obtained from redshift, and CALIFA data quality flags from the Third Data Release (Sánchez et al. 2016a). The contents of this table are summarized in Table 1. As noted in Sánchez et al. (2016b), `Pipe3D` uses the `gsd156` stellar library from Cid Fernandes et al. (2013), adopting a Salpeter (1955) stellar initial mass function (IMF), which we adopt for consistency throughout the database.

Figure 1, derived from the CALIFA global table, shows the location of our sample galaxies in the conventional main-sequence diagram of SFR versus stellar mass (M_*), and the

[16] https://github.com/tonywong94/edge_pydb

[17] http://leda.univ-lyon1.fr

[18] http://ned.ipac.caltech.edu

Table 1
Description of Columns in the CALIFA Global Table

Col. Name	Units	Description
ID	⋯	CALIFA ID number
Name	⋯	Galaxy name
caSu	mag	SDSS u magnitude from CALIFA synthetic photometry
caSg	mag	SDSS g magnitude from CALIFA synthetic photometry
caSr	mag	SDSS r magnitude from CALIFA synthetic photometry
caSi	mag	SDSS i magnitude from CALIFA synthetic photometry
caB	mag	B magnitude from CALIFA synthetic photometry
caV	mag	V magnitude from CALIFA synthetic photometry
caR	mag	R magnitude from CALIFA synthetic photometry
caRe	arcsec	Equivalent galactocentric radius Re from CALIFA photometry
caeRe	arcsec	Error in equivalent galactocentric radius from CALIFA photometry
caEllipticity	⋯	Ellipticity $\sqrt{(1 - b^2/a^2)}$ from CALIFA photometry
caPA	deg	Position angle from CALIFA photometry
caR50	arcsec	R50 (radius enclosing 50% flux) from CALIFA photometry
caeR50	arcsec	Error in R50 from CALIFA photometry
caR90	arcsec	R90 (radius enclosing 90% flux) from CALIFA photometry
caeR90	arcsec	Error in R90 from CALIFA photometry
cazgas	⋯	Redshift for gas lines from `z_gas` in get_proc_elines table
cazstars	⋯	Redshift for stars from `z_stars` in get_proc_elines table
caAge	dex (Gyr)	Mean stellar age from `log_age_mean_LW` in get_proc_elines
caeAge	dex (Gyr)	Error in mean stellar age from `s_log_age_mean_LW` in get_proc_elines
caFHa	dex (10^{-16} erg cm^{-2} s^{-1})	Log of Hα flux from `log_F_Ha` in get_proc_elines
caFHacorr	dex (10^{-16} erg cm^{-2} s^{-1})	Log of extinction-corrected Hα flux from `log_F_Ha_cor` in get_proc_elines
caLHacorr	dex (erg s^{-1})	Log of extinction-corrected Hα luminosity from `log_L_Ha_cor` in get_proc_elines
caMstars	dex ($M_\odot$)	Log of stellar mass from `log_Mass` in get_proc_elines
caeMstars	dex ($M_\odot$)	Error in log of stellar mass from `error_Mass` in get_proc_elines
caSFR	dex ($M_\odot$ yr^{-1})	SFR from `lSFR` in get_proc_elines
caeSFR	dex ($M_\odot$ yr^{-1})	Error in SFR from `e_lSFR` in get_proc_elines
caOH	dex	Oxygen abundance as 12+log(O/H) from `OH_O3N2` in get_proc_elines
caeOH	dex	Error in oxygen abundance from `e_OH_O3N2` in get_proc_elines
caAvgas	mag	Nebular extinction as Av from `Av_gas_LW_Re` in get_proc_elines
caeAvgas	mag	Error in nebular extinction from `e_Av_gas_LW_Re` in get_proc_elines
caAvstars	mag	Stellar extinction as Av from `Av_ssp_stats_mean` in get_proc_elines
caeAvstars	mag	Error in stellar extinction `Av_ssp_stats_stddev` in get_proc_elines
caDistP3d	Mpc	Luminosity distance in Mpc used by Pipe3D, from `DL` in get_proc_elines
caDistMpc	Mpc	Luminosity distance in Mpc from `cazgas` assuming $H_0 = 70$, $\Omega_m = 0.27$, $\Omega_\Lambda = 0.73$
caFlgWav5	⋯	Flag ($-1/0/1/2$ = NA/good/minor/bad) for wavelength calibration in V500
caFlgWav12	⋯	Flag ($-1/0/1/2$ = NA/good/minor/bad) for wavelength calibration in V1200
caFlgReg5	⋯	Flag ($-1/0/1/2$ = NA/good/minor/bad) for 2D registration rel to SDSS in V500
caFlgReg12	⋯	Flag ($-1/0/1/2$ = NA/good/minor/bad) for 2D registration rel to SDSS in V1200
caFlgImg5	⋯	Flag ($-1/0/1/2$ = NA/good/minor/bad) for reconstructed image quality in V500
caFlgImg12	⋯	Flag ($-1/0/1/2$ = NA/good/minor/bad) for reconstructed image quality in V1200

strong observed correlation between a galaxy's offset from the main sequence and the observed molecular gas to stellar mass ratio. This figure demonstrates that molecular gas content has a strong effect on the location of a galaxy relative to the main sequence.

Derived parameters. These include galaxy properties derived from analyses conducted by the EDGE team. Examples include orientation parameters and systemic velocities from rotation curve fitting (Leung et al. 2018; Levy et al. 2018) and half-light radii derived from integrating flux in elliptical rings (Bolatto et al. 2017).

2.4. CO Image Tables

The image tables (saved in HDF5 format) are obtained by sampling FITS images. For the matching of the CARMA and CALIFA data, the coordinate grid is established by the original CO cubes, which were imaged with 1″ pixels in an orthographic projection in J2000 coordinates. The spatial extent of the cubes has been truncated to 128×128 pixels; this is sufficient to cover both the CARMA and CALIFA fields of view. In addition to the CO cubes themselves, we sample the moment images that are derived from the cubes following a masking process. Three different masking approaches are employed, with the results from each approach saved in a separate table (*path*) in the HDF5 file. The paths are labeled as follows:

1. `comom_str`. This is a *straight* moment calculation (no masking employed). Only the zeroth moment (integrated intensity) is included, as the higher moments are largely unusable due to noise in the spectrum. Even the zeroth moment is typically dominated by noise and is useful primarily as a rough guide to what signal would be clearly detected in the absence of any masking.
2. `comom_dil`. The data are first masked using a *dilated* approach (expanding from a 3.5σ threshold over two

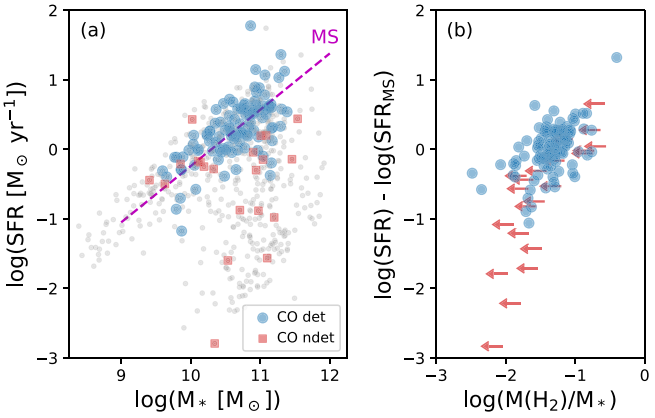

Figure 1. (a) Location of EDGE-CALIFA sample in a plot of SFR vs. M_*. The dashed magenta line shows the approximate locus of the star-forming main sequence from Cano-Díaz et al. (2016). CO nondetections are indicated by red squares. Small gray dots are used to represent the full CALIFA DR3 sample. (b) Vertical offset from the star-forming main sequence as a function of molecular to stellar mass ratio. The two quantities are correlated, underscoring the importance of gas content for continued star formation. CO nondetections (2σ upper limits) are indicated by horizontal arrows.

consecutive channels out to a 2σ threshold, with a minimum area of two synthesized beams for each mask region) before the moments are calculated. For ^{13}CO, the dilated mask from the CO cube is applied. This table also includes the peak signal-to-noise ratio (S/N) images as `snrpk_12` and `snrpk_13`. Although these are constructed without masking (and should thus logically be included in the `comom_str` table), they are included in this table as most users will adopt the dilated masks for initial data inspection.

3. `comom_smo`. This is a *smoothing* approach where the cube is first convolved to a resolution of 14″ before generating a dilated mask as described above. This generally yields a more permissive mask than `comom_dil`, which is then applied to the unsmoothed data before the moments are calculated. For ^{13}CO, the corresponding mask from the CO cube is applied.

For both *dilated* and *smoothed* approaches, an additional mask expansion of 1 pixel in 3D (2 pixels for the smoothed approach) is introduced to pick up additional weak emission. Since the masks are 3D, they are included with the cube data rather than the image tables. The overall approach to moment map generation remains as described by Bolatto et al. (2017), but using a Python implementation (`maskmoment`[19]) to remove a previous dependency on IDL.

Figure 2 shows how the masking methods compare for NGC 4047. The tables above also include estimates of molecular gas surface density (`sigmol`) derived from the CO moment-0 values by applying a constant CO-to-H_2 conversion factor (see Section 2.6.3). Note that the tabulated intensities and surface densities have *not* been deprojected to face-on values, although a `cosi` column (representing the cosine of the inclination) is provided, which can be multiplied by any column to yield a deprojected value based on the LEDA-derived inclination (Section 2.3). A summary of the columns currently provided in the `comom_dil` table is provided in Table 2.

[19] https://github.com/tonywong94/maskmoment

2.5. CALIFA Image Tables

For the CALIFA data, we sample a subset of the Pipe3D analysis products rather than the IFU cubes directly. Separate tables ("paths") for the Pipe3D products labeled as `ELINES`, `flux_elines`, `SFH`, `SSP`, and `indices` (see Sánchez et al. 2016b) are provided. Each of these products is ingested as an FITS file (or as an extension in a multiextension FITS file), which is essentially a concatenation of individual images into a pseudo-cube. Tables 3 and 4 summarize the columns that are provided in the `SSP` and `flux_elines` tables. Pipe3D was run on two sets of cubes, the native-resolution DR3 cubes and a set of cubes obtained by convolving the DR3 cubes to a Gaussian point-spread function (PSF; 7″ FWHM) to match the CARMA data. To perform the convolution, we model the CALIFA PSF as a Moffat profile with the characteristics provided in the FITS header; in cases where this was not available, we assume a Moffat profile with FWHM 2.″5 and $\beta_M = 2.15$, which represent the mean and weighted median of the CALIFA DR3 sample as measured by Sánchez et al. (2016a). We store the native and convolved data in separate HDF5 files as detailed below. The images that are matched to the CARMA resolution have been interpolated onto the CARMA astrometric grid, using nearest-neighbor sampling in the `reproject` Python package, before pixel extraction.

2.5.1. Full-pixel Databases

For the users who wish to recover all pixels from the FITS images, at the cost of significant oversampling, we provide large HDF5 files that contain the complete set of 1 arcsec^2 pixel values in a tabular format. The `edge_carma_allpix.pipe3d.hdf5` file contains all pixels in the native-resolution Pipe3D images, without regridding to match the CARMA astrometry. The `edge_carma_allpix.2d_smo7.hdf5` file, which was used to generate Figure 2, contains all pixels in the matched (7″ FWHM) resolution CO and Pipe3D images, with CARMA and CALIFA data placed in separate *paths* (tables) in the HDF5 file.

2.5.2. Square Grid Downsampling

Given that a Gaussian beam with FWHM 7″ spans an area of 55.5 arcsec^2, we are heavily oversampling the beam with our 1″ pixels. We therefore generate smaller tables, which sample one of every three pixels in R.A. and decl. (3″ spacing), reducing the number of pixels per galaxy from 128^2 to 43^2 (a factor of 8.9). We still cover each beam area with slightly more than six sampling pixels. Combining the 125 galaxies, the image tables contain $43^2 \times 125 = 231\,125$ rows of sampled image data. The `edge_carma.2d_smo7.hdf5` file contains these extracted pixels from the matched-resolution CO and Pipe3D images. The `edge_carma.cocube_smo7.hdf5` file contains the corresponding CO spectra and CO mask information at the extracted pixels.

2.5.3. Hexagonal Grid Sampling

In addition to the square grid, we have also implemented an option to sample the CARMA and CALIFA data on a hexagonal grid (file `edge_carma_hex.2d_smo7.hdf5`). For a uniform hexagonal grid, the minimum spacing between grid points can be increased by a factor of $2/\sqrt{3}$ compared to a square grid while still achieving the same level of

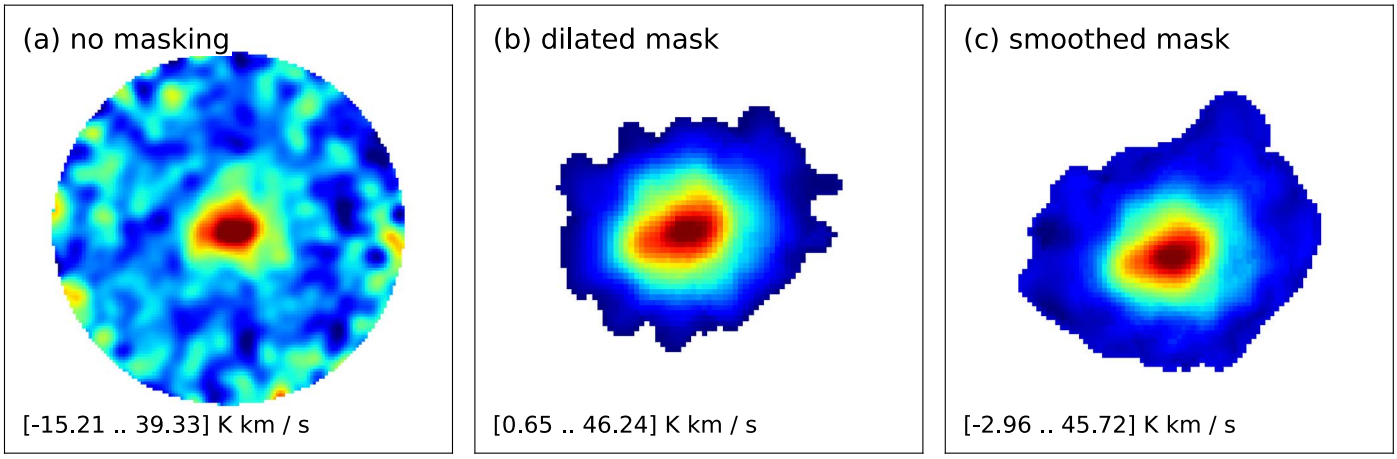

Figure 2. Integrated CO intensity (moment-0) maps of NGC 4047, obtained with (a) no masking; (b) a dilated mask expanding from a 3.5σ threshold over 2 consecutive channels out to a 2σ threshold; and (c) a smoothed mask where the cube is convolved to 14″ FWHM before a dilated mask is generated. Each panel is approximately 147″ square. The colormap range is shown at the bottom of each panel.

Table 2
Description of Columns in the comom_dil Table

Col. Name	Units	Description	n_bad[a]
Name	⋯	Galaxy name	0
ix	⋯	0-based pixel index in *x*-direction	0
iy	⋯	0-based pixel index in *y*-direction	0
ra_abs	deg	Sample R.A. coordinate	0
dec_abs	deg	Sample decl. coordinate	0
ra_off	deg	R.A. offset from reference pixel	0
dec_off	deg	Decl. offset from reference pixel	0
rad_arc	arcsec	Galactocentric radius based on LEDA	0
azi_ang	deg	Azimuthal angle based on LEDA	0
snrpk_12	⋯	CO peak signal-to-noise ratio	705
mom0_12	K km s^{-1}	CO integrated intensity using dilated mask	1657
e_mom0_12	K km s^{-1}	CO error in mom0 assuming dilated mask	1657
mom1_12	km s^{-1}	CO intensity weighted mean velocity using dilated mask	1670
e_mom1_12	km s^{-1}	CO error in mom1 assuming dilated mask	1670
mom2_12	km s^{-1}	CO intensity weighted vel disp using dilated mask	1694
e_mom2_12	km s^{-1}	CO error in mom2 assuming dilated mask	1694
sigmol	$M_\odot$ pc^{-2}	Apparent H_2+He surface density (not deprojected)	1657
e_sigmol	$M_\odot$ pc^{-2}	Error in sigmol (not deprojected)	1657
cosi	⋯	Factor to deproject to face-on using ledaAxIncl	0
snrpk_13	⋯	^{13}CO peak signal-to-noise ratio	648
mom0_13	K km s^{-1}	^{13}CO integrated intensity using dilated mask	1657
e_mom0_13	K km s^{-1}	^{13}CO error in mom0 assuming dilated mask	1657
mom1_13	km s^{-1}	^{13}CO intensity weighted mean velocity using dilated mask	1673
e_mom1_13	km s^{-1}	^{13}CO error in mom1 assuming dilated mask	1670
mom2_13	km s^{-1}	^{13}CO intensity weighted vel disp using dilated mask	1731
e_mom2_13	km s^{-1}	^{13}CO error in mom2 assuming dilated mask	1731

Note.
[a] Number of undefined pixels for NGC 4047, out of a maximum of $43^2 = 1849$. This will differ among galaxies and is only listed for illustrative purposes.

oversampling. Multiplying this factor by 3″ yields a 3.″5 spacing between adjacent hexagonal cells. The reference pixel of the CO image is placed at the (0,0) position of the grid. The grid is constructed using two vectors as shown in Figure 3. The hexagonal cells are created first along the diagonal line and then created in the vertical directions.

Interpolation of the original square pixel values onto the grid is done by calculating the distance from the center of the hexagon to the centers of the four nearest pixels, then weighting the pixel values by the inverse distance. This approach differs slightly from the hexagonally sampled SQL database, which also uses a 3.″5 nearest-neighbor spacing but does not apply interpolation, instead adopting the value of the 1″ pixel closest to each hexagonal grid point. A comparison of the three different sampling approaches (all pixels, square grid sampling, and hexagonal grid sampling) is provided in Figure 4. The comparison shows that the latter two sampling methods provide largely equivalent information compared to that of the full-pixel sampling in a much more compact data format.

Table 3
Description of Columns in the SSP Table

Col. Name	Units	Description	n_bad
Name	⋯	Galaxy Name	0
ix	⋯	0-based pixel index in *x*-direction	0
iy	⋯	0-based pixel index in *y*-direction	0
...	...	...	...
Vcont_ssp_sm	10^{-16} erg Å^{-1} s^{-1} cm^{-2}	Pseudo *V*-band map	1395
cont_segm_sm	⋯	Continuum segmentation file	1395
cont_dezon_sm	⋯	Continuum dezonification file	1395
medflx_ssp_sm	10^{-16} erg Å^{-1} s^{-1} cm^{-2}	Median intensity flux within the wavelength range	1395
e_medflx_ssp_sm	10^{-16} erg Å^{-1} s^{-1} cm^{-2}	Error in median intensity flux within the wavelength range	1395
age_lwt_sm	dex (yr)	Luminosity weighted age of the stellar population	1395
age_mwt_sm	dex (yr)	Mass weighted age of the stellar population	1395
e_age_lwt_sm	⋯	Error in age of the stellar population	1395
ZH_lwt_sm	dex	Luminosity weighted metallicity of the stellar population	1395
ZH_mwt_sm	dex	Mass weighted metallicity of the stellar population	1395
e_ZH_lwt_sm	⋯	Error in metallicity of the stellar population	1395
Av_ssp_sm	mag	Average dust attenuation of the stellar population	1395
e_Av_ssp_sm	mag	Error in the average dust attenuation of the stellar population	1395
vel_ssp_sm	km s^{-1}	Velocity of the stellar population	1395
e_vel_ssp_sm	km s^{-1}	Error in the velocity of the stellar population	1395
vdisp_ssp_sm	km s^{-1}	Velocity dispersion of the stellar population	1395
e_vdisp_ssp_sm	km s^{-1}	Error in velocity dispersion of the stellar population	1395
ML_ssp_sm	$M_\odot\ L_\odot^{-1}$	Average mass-to-light ratio of the stellar population	1395
mass_ssp_sm	dex ($M_\odot$ arcsec^{-2})	Stellar mass density	1395
mass_Avcor_ssp_sm	dex ($M_\odot$ arcsec^{-2})	Stellar mass density dust corrected	1395
sigstar_sm	$M_\odot$ pc^{-2}	Stellar mass surface density	1395
sigstar_Avcor_sm	$M_\odot$ pc^{-2}	Stellar mass surface density dust corrected	1395
fe_medflx_sm	⋯	Fractional error in continuum flux	1395
sigsfr_ssp_sm	$M_\odot$ Gyr^{-1} pc^{-2}	Sigma_SFR from < 32 Myr SSP	1395
sigsfr_Avcor_ssp_sm	$M_\odot$ Gyr^{-1} pc^{-2}	Sigma_SFR Av-corrected from <32 Myr SSP	1395

2.6. Derived Quantities and Uncertainties

In addition to the CO intensity data and the Pipe3D output, we include additional derived columns in the database as described below.

2.6.1. Star Formation Surface Density

The star formation surface density $\Sigma_{\rm SFR}$ is derived from Hα surface brightness using the conversion factor from Equation (5) of Calzetti et al. (2010), but with the numerical coefficient scaled by 1.51 to convert from a Kroupa et al. (1993) IMF to the Salpeter (1955) IMF employed by Pipe3D:

$$\mathrm{SFR}[M_\odot\ \mathrm{yr}^{-1}] = 8.23 \times 10^{-42}\, L(\mathrm{H}\alpha)\ [\mathrm{erg\ s}^{-1}]. \quad (1)$$

Three separate estimates are calculated. The first estimate (`sigsfr0`) assumes no extinction and simply rescales the Hα surface brightness, converting it to a luminosity surface density assuming each patch of the galaxy radiates isotropically. The fractional error in this quantity is just the fractional error in the Hα surface brightness. The second estimate (`sigsfr_corr`) corrects the SFR for extinction, $A(\mathrm{H}\alpha)$, as obtained from the Balmer decrement (e.g., Catalán-Torrecilla et al. 2015):

$$A(\mathrm{H}\alpha) = \frac{K_{\mathrm{H}\alpha}}{-0.4(K_{\mathrm{H}\alpha} - K_{\mathrm{H}\beta})} \times \log_{10}\frac{I(\mathrm{H}\alpha)}{2.86\, I(\mathrm{H}\beta)}, \quad (2)$$

where we adopt $K_{\mathrm{H}\alpha} = 2.53$, and $K_{\mathrm{H}\beta} = 3.61$ based on the extinction curve of Cardelli et al. (1989). The uncertainty in this quantity is determined by propagating the errors of the Hα and Hβ intensities assuming these errors are uncorrelated. The third estimate (`sigsfr_adopt`) applies spatial smoothing (by a 2D Gaussian kernel with a standard deviation of 3″) to the Hα and Hβ images before their ratio is taken to obtain the Balmer

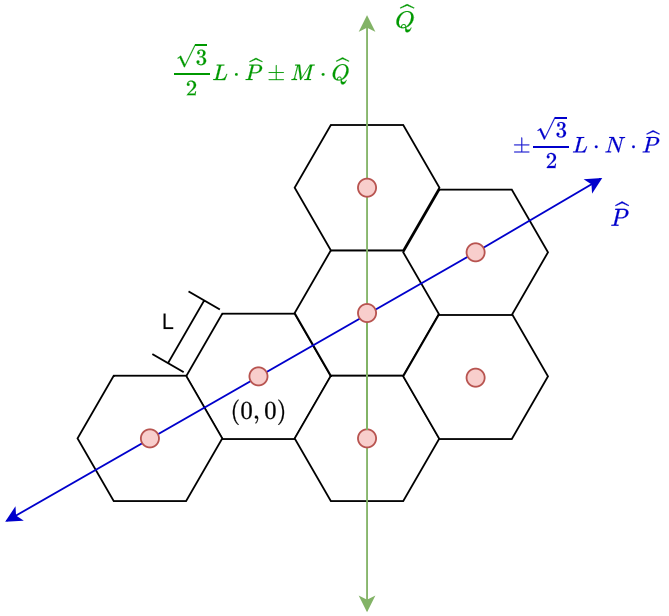

Figure 3. The construction of the hexagonal grid. L is the side length of the hexagon and can be set by the user. Blue and green vectors form the basis used to construct the grid. Hexagons are first created along the diagonal, following the blue vector $\hat{P}$. Then, for each hexagon along $\hat{P}$, additional hexagons are created following the green vertical vector $\hat{Q}$.

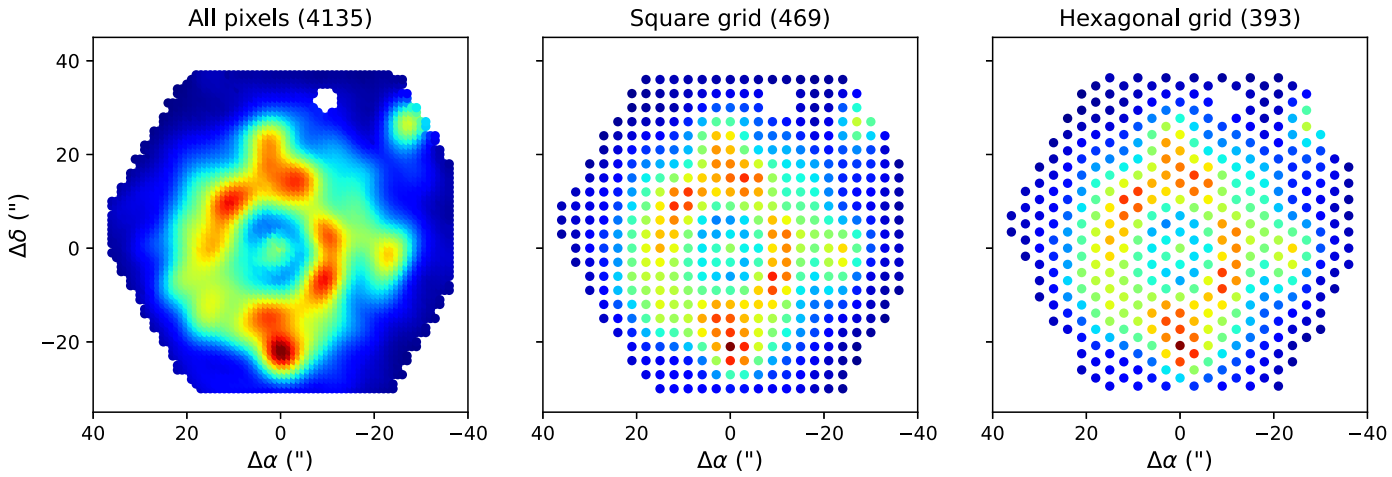

Figure 4. Comparison of the three sampling methods in the edge_pydb, using the Hα image of NGC 3687 as an example. Counts of unblanked pixels are given in parentheses.

Table 4
Description of Columns in the flux_elines Table

Col. Name	Units	Description	n_bad
Name	⋯	Galaxy name	0
ix	⋯	0-based pixel index in *x*-direction	0
iy	⋯	0-based pixel index in *y*-direction	0
...	...	...	...
flux_Hbeta_sm	10^{-16} erg s^{-1} cm^{-2}	Hβ intensity	1386
flux_Halpha_sm	10^{-16} erg s^{-1} cm^{-2}	Hα intensity	1386
vel_Hbeta_sm	km s^{-1}	Hβ velocity	1386
vel_Halpha_sm	km s^{-1}	Hα velocity	1386
disp_Hbeta_sm	Å	Hβ velocity dispersion	1386
disp_Halpha_sm	Å	Hα velocity dispersion	1386
EW_Hbeta_sm	Å	Hβ equivalent width	1386
EW_Halpha_sm	Å	Hα equivalent width	1386
e_flux_Hbeta_sm	10^{-16} erg s^{-1} cm^{-2}	Error in Hβ intensity	1386
e_flux_Halpha_sm	10^{-16} erg s^{-1} cm^{-2}	Error in Hα intensity	1386
e_vel_Hbeta_sm	km s^{-1}	Error in Hβ velocity	1386
e_vel_Halpha_sm	km s^{-1}	Error in Hα velocity	1386
e_disp_Hbeta_sm	Å	Error in Hβ velocity dispersion	1386
e_disp_Halpha_sm	Å	Error in Hα velocity dispersion	1386
e_EW_Hbeta_sm	Å	Error in Hβ equivalent width	1386
e_EW_Halpha_sm	Å	Error in Hα equivalent width	1386
flux_Hbeta_sm3_sm	10^{-16} erg s^{-1} cm^{-2}	Hβ intensity after 3 pix smooth	1386
flux_Halpha_sm3_sm	10^{-16} erg s^{-1} cm^{-2}	Hα intensity after 3 pix smooth	1386
flux_sigsfr0_sm	$M_\odot$ Gyr^{-1} pc^{-2}	SFR surface density no extinction	1386
e_flux_sigsfr0_sm	$M_\odot$ Gyr^{-1} pc^{-2}	Error of uncorrected SFR surface density	1386
flux_sigsfr_corr_sm	$M_\odot$ Gyr^{-1} pc^{-2}	Balmer-decrement (BD)-corrected SFR surface density	1387
e_flux_sigsfr_corr_sm	$M_\odot$ Gyr^{-1} pc^{-2}	Error of BD-corrected SFR surface density	1387
flux_AHa_corr_sm	mag	Hα extinction from BD	1387
e_flux_AHa_corr_sm	mag	Error of Hα extinction from BD	1387
flux_AHa_smooth3_sm	mag	Hα extinction after 3 pix smooth	1386
flux_sigsfr_adopt_sm	$M_\odot$ Gyr^{-1} pc^{-2}	Smooth+clip BD-corrected SFR surface density	1386
BPT_sm	⋯	BPT type (-1 = SF 0 = inter 1 = LINER 2 = Sy)	1397
p_BPT_sm	⋯	BPT probability	1397
SF_BPT_sm	⋯	True if star-forming (BPT = -1 and EW_Ha > 6)	0
ZOH_sm	dex	12+log(O/H) using O3N2 method in Marino+13	1489
e_ZOH_sm	dex	Error in 12+log(O/H) using O3N2 method in Marino+13	1489

decrement. Smoothing reduces the noise in the resulting estimate of A(Hα), increasing the fraction of inferred A(Hα) values between 0 and 2 mag from 54% to 60%; for spaxels classified as star-forming, this fraction increases from 78% to 85%. This comes at the cost of some inconsistency between the coarser resolution A(Hα) images and the 7″ resolution Hα images that are being corrected. We use the unsmoothed error maps for Hα and Hβ when propagating the uncertainty for `sigsfr_adopt`.

None of the error estimates for $\Sigma_{\rm SFR}$ take into account uncertainties in the extinction curve, IMF, or other factors

needed to convert from the recombination line flux to SFR. When the inferred $A(\mathrm{H}\alpha) < 0$, we do not make an extinction correction, instead falling back on `sigsfr0` and its uncertainty. The values are blanked (set to NaN) when the inferred $A(\mathrm{H}\alpha) > 6$.

2.6.2. Stellar Surface Density

The `SSP` table (denoting the results of a simple stellar population analysis) provided by Pipe3D provides a column `mass_ssp` that provides the stellar mass derived by Pipe3D for each 1 arcsec^2 CALIFA spaxel. We add an additional `sigstar` column that converts this value to $M_\odot$ pc^{-2} using the galaxy distance adopted by Pipe3D. The corresponding dust-corrected estimates `mass_AVcor_ssp` and `sigstar_Avcor` are also provided; these make use of A_V derived from the stellar population analysis, which can differ significantly from the Balmer-decrement-derived extinction. Although Pipe3D does not provide formal uncertainties for `mass_ssp` or `mass_AVcor_ssp`, the fractional error in the continuum flux (`fe_medflux`) can be used as a rough estimate.

The resolved star formation history provided by the `SFH` table (in bins of age and metallicity) is also used to provide two estimates of Σ_{SFR} that are included in the `SSP` table. These estimates are computed by taking the mass fraction at ages <32 Myr (summed over metallicity), scaling by either `sigstar` or `sigstar_Avcor`, and dividing the result by 32 Myr. The choice of summing time bins up to 32 Myr to measure the "young" stellar population provides a compromise between time resolution and smoothing over the large uncertainties involved in stellar population modeling (see González Delgado et al. 2016 for further discussion).

2.6.3. Molecular Gas Surface Density

The molecular gas surface density Σ_{mol}, including H_2 and associated helium, is derived by multiplying the CO surface brightness with a Galactic value for the CO-to-H_2 conversion factor (e.g., Bolatto et al. 2013):

$$\alpha_{\mathrm{CO}} = 4.3\, M_\odot\, (\mathrm{K\ km\ s^{-1}\ pc^2})^{-1}. \tag{3}$$

This column is provided as `sigmol` in the `comom_xxx` (e.g., `comom_dil`) table. As noted in Section 2.4, an additional column `cosi` contains the multiplicative factor needed to deproject the surface density to face-on assuming a plane-parallel disk. If used for comparative analysis, the $\cos i$ factor should be used to deproject other surface densities as well.

The use of a constant CO-to-H_2 conversion factor is obviously a simplification, and a number of studies have inferred a decrease of the conversion factor at stellar surface densities of $\gtrsim 100 M_\odot$ pc^{-2} (e.g., Chiang et al. 2024) and an increase in the conversion factor at low metallicities (e.g., Accurso et al. 2017). We have elected not to implement a variable conversion factor in the current database, for two reasons. First, the fraction of $\Sigma_* > 100\, M_\odot\, \mathrm{pc}^{-2}$ points is relatively small (∼20%), and even above this limit, the inferred dependence on Σ_* is relatively weak for the CO(1–0) line ($\propto \Sigma_*^{-0.3}$). Second, the metallicity range for star-forming spaxels in the EDGE-CALIFA sample is relatively limited (spanning about 0.2 dex or a factor of 1.6) and comparable in size to the systematics in oxygen metallicity calibrations (Marino et al. 2013). We therefore defer the implementation of a variable conversion factor to a future work that can examine a wider range of conditions.

2.6.4. Oxygen Abundance

We determine the gas-phase metallicity by taking a ratio of two emission-line ratios, [O III]λ5007/Hβ and [N II]λ6583/Hα (i.e., the O3N2 method; Alloin et al. 1979; Pettini & Pagel 2004). We use the following prescription from Marino et al. (2013):

$$12 + \log(\mathrm{O/H}) = 8.533 - 0.214 \log\left(\frac{[\mathrm{O\ III}]}{\mathrm{H}\beta} \times \frac{\mathrm{H}\alpha}{[\mathrm{N\ II}]}\right), \tag{4}$$

which has been derived for the logarithm ranging from −1 to 1.7, encompassing the range of our data. Since the metallicity calibration is reliant upon the emission lines arising from H II regions, we also require a *star-forming* Baldwin–Phillips–Terlevich (BPT) classification (`SF_BPT` flag in Section 2.6.5 below); otherwise, the value is blanked. The error propagation is performed using a standard approach taking into account only the uncertainties in the emission-line fluxes and assuming they are independent. The resulting values are saved as the `ZOH` column in the `flux_elines` table (Table 4).

2.6.5. BPT Classification of Pixels

The same line ratios used to estimate metallicity can also provide useful insight into the nature of ionized regions in galaxies. This is the basis of the most widely used "BPT" diagram (Baldwin et al. 1981), which plots [O III]λ5007/Hβ against [N II]λ6583/Hα. From exploring a wide range of parameters in photoionization models, Kewley et al. (2001) deduced that star-forming regions must lie below a curve defined by the equation

$$\log\left(\frac{[\mathrm{O\ III}]}{\mathrm{H}\beta}\right) = 1.19 + \frac{0.61}{\log([\mathrm{N\ II}]/\mathrm{H}\alpha) - 0.47}. \tag{5}$$

Based on spectra from the SDSS, Kauffmann et al. (2003) introduced a more restrictive condition for star-forming regions, which is that they argued typically lie below the curve defined by

$$\log\left(\frac{[\mathrm{O\ III}]}{\mathrm{H}\beta}\right) = 1.3 + \frac{0.61}{\log([\mathrm{N\ II}]/\mathrm{H}\alpha) - 0.05}. \tag{6}$$

Finally, in the upper right part of the BPT diagram, signifying harder radiation fields, Cid Fernandes et al. (2010) find that Seyfert nuclei tend to lie above the line

$$\log\left(\frac{[\mathrm{O\ III}]}{\mathrm{H}\beta}\right) = 0.48 + 1.01 \log\left(\frac{[\mathrm{N\ II}]}{\mathrm{H}\alpha}\right), \tag{7}$$

with the points falling below this line characterized as LINERs (although such line ratios are by no means exclusively found in nuclear regions, e.g., Belfiore et al. 2016). Following standard convention, we classify points below the Kauffmann et al. (2003) curve as consistent with star-forming (BPT code −1); points between the Kauffmann et al. (2003), Kewley et al. (2001) curves as intermediate or composite (BPT code 0); points above the Kewley et al. (2001) curve and below the Cid

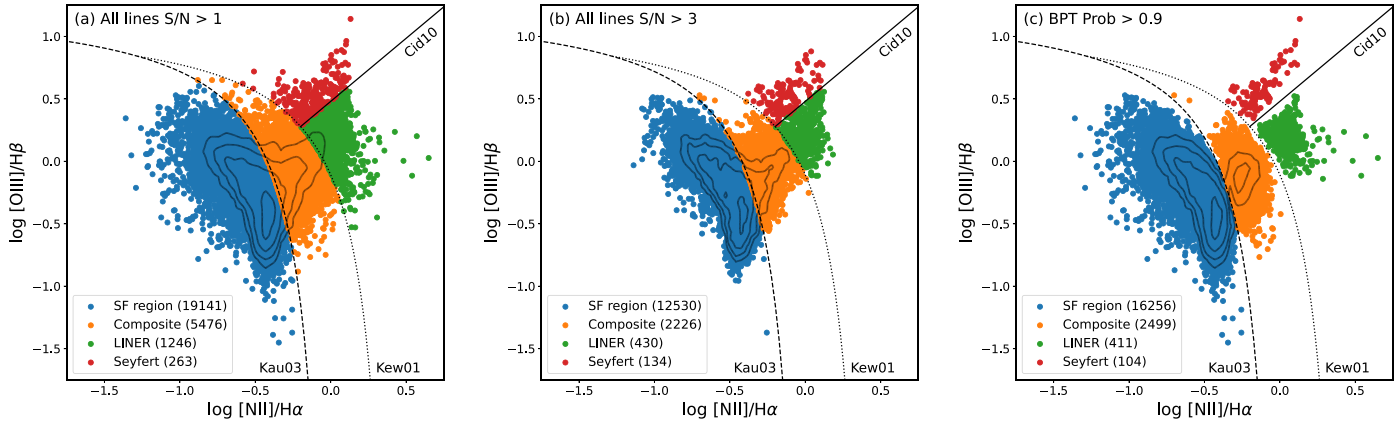

Figure 5. Comparison between BPT plots with different selection cuts applied. (a) All EDGE samples plotted where each of the four emission-line fluxes exceeds its 1σ uncertainty. (b) Points from (a) where each line's flux exceeds 3σ. (c) Points from (a) where the BPT probability estimate exceeds 0.9. Gray contours indicate the density of points. Demarcation lines defined by Kewley et al. (2001), Kauffmann et al. (2003), and Cid Fernandes et al. (2010) are shown as dashed, dotted, and solid curves respectively.

Fernandes et al. (2010) line as LINER (BPT code 1); and points above the Kewley et al. (2001) curve and above the Cid Fernandes et al. (2010) line as Seyfert (BPT code 2). The BPT code for each sample pixel is included as a column in the `flux_elines` table, and an additional `SF_BPT` column is set to true when the BPT code is -1 and the Hα equivalent width exceeds 6 Å; we consider such regions as very likely to be star-forming (e.g., Barrera-Ballesteros et al. 2018).

To assist with interpreting the distribution of points in the diagram, we implemented a probability calculation algorithm for the BPT types. The flux uncertainties for [N II], [O III], Hα, and Hβ are used to calculate the probability that a data point actually lies within the region of the BPT diagram that it is assigned to. This calculation is done by constructing a bivariate Gaussian error distribution assuming independent errors, and numerically estimating the fractional area of the Gaussian that lies in the same BPT region as the center of the Gaussian. In practice, this is done by sampling points in the distribution using a 5×5 grid spanning $\pm 1\sigma$ around the nominal value. Panels (b) and (c) of Figure 5 show how a simple S/N cut applied to the four emission lines compares with imposing the condition that the BPT probability exceeds 0.9. A probability criterion allows more uncertain points to be considered as long as they lie safely within their designated BPT region. On the other hand, a probability criterion does reject the points that lie close to the demarcation lines or where the BPT regions themselves span a narrow extent, since the resulting classification is deemed more uncertain.

2.7. Azimuthally Aggregated Data

The 1D radial profile data are obtained from analysis of the original FITS images and provided as plain text tables. These include radial CO profiles derived from the "smoothed" mask moment-0 maps, as well as circular velocity curves derived from the analysis of Leung et al. (2018) for CO and Levy et al. (2018) for CO and Hα. The CO radial profiles and rotation curves are plotted for the subset of 54 EDGE galaxies studied by Leung et al. (2018) in Figures 6 and 7 respectively.

Radial CO brightness profiles (deprojected to face-on) are calculated for galaxies with inclinations $<85°$ by averaging in concentric rings after setting masked pixels to zero; only rings with 10% or greater valid pixels are tabulated. The less restrictive *smoothed* moment masks are used in order to include more pixels in the averaging. The ring widths used are $2''$ for the native-resolution cubes and $3''$ for the common resolution ($7''$) cubes. The error bars on the points represent the rms deprojected value within the ring for unmasked pixels. A 3σ detection limit profile, derived from collapsing and azimuthally averaging the rms noise cube over a 200 km s^{-1} velocity width (or using the actual mask width if larger), is shown as a black dashed line in Figure 6; this is higher near the galaxy center where fewer independent beams contribute to the azimuthal average. Note that the radial profiles may underestimate the true brightness profiles because faint CO emission may still be present at the masked pixels. Simple alternatives, such as not employing any masking, yield poorer results due to negative residuals in the CO cubes. A more sensitive approach is to use the Hα velocity field to align and stack CO spectra, as presented by Villanueva et al. (2021). To derive a radial intensity profile, the stacked spectra are integrated over a velocity window that becomes narrower with increasing galactocentric radius; this is equivalent to using the Hα velocity to define the centroid of a signal mask and the galactocentric radius to specify the mask's velocity width.

Rotation curves are also deprojected to represent circular velocities v_c, although we plot $v_c \sin i$ in Figure 7 to allow more straightforward comparison of analyses where different inclination angles have been assumed. In addition to providing the curves previously published by Leung et al. (2018), Levy et al. (2018), we have derived new CO rotation curves for 79 galaxies using the `3D-Barolo` software (Di Teodoro & Fraternali 2015) applied to 10 km s^{-1} channel cubes with the primary beam pattern normalized out (so the noise does not rise toward the edge of the field). The fits were performed with the center position and disk inclination fixed to their LEDA values and in two passes where the first pass determines an average position angle and systemic velocity across all available rings, and the second pass determines the circular speed and gas velocity dispersion (assumed isotropic) of each ring. The latter quantity, $\sigma_v(R)$, is not typically available from an analysis of velocity images alone. The database provides fit results for both passes as separate ECSV files, and provides global orientation parameters for each galaxy as an additional table

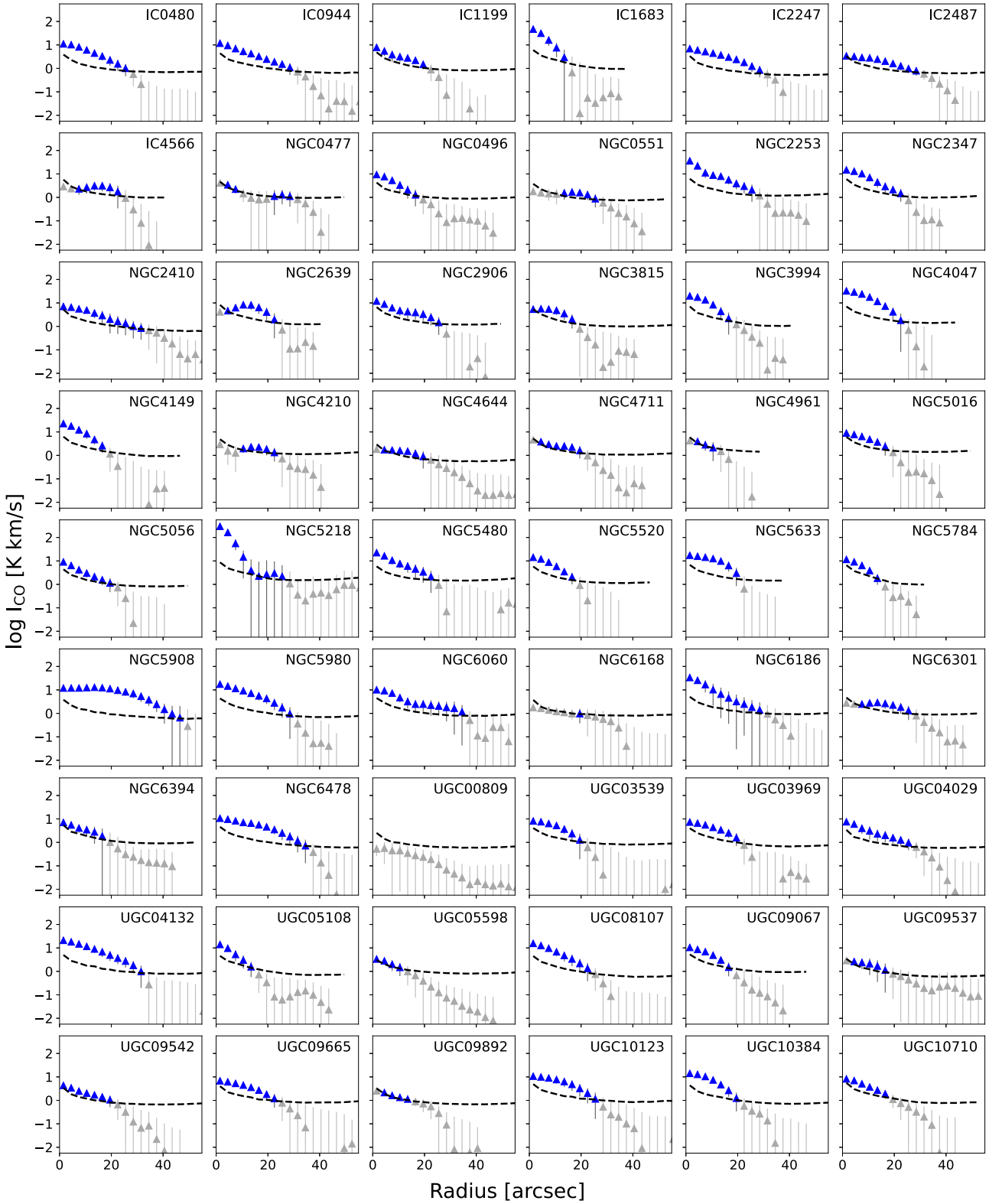

Figure 6. Inclination-corrected radial CO profiles for the sample of 54 galaxies studied by Leung et al. (2018). The dashed curve in each panel represents a 3σ detection limit adopting a default velocity width of 200 km s^{-1} but using the actual mask width where it exceeds 200 km s^{-1} in width. Gray points denote radii where the azimuthal average is measured (i.e., there are >10% unmasked CO pixels at these radii) but falls below the detection limit and is thus unreliable.

`edge_bbpars_smo7.csv`. While `3D-Barolo` implicitly takes beam smearing into account by convolving its model with the synthesized beam before a comparison with the data, it can have difficulty distinguishing between a steeply rising rotation curve near the nucleus and an increase in velocity dispersion there, so the sharp rise in circular speed inferred near the centers of some galaxies may be spurious. Overall, Figure 7 suggests that the `3D-Barolo` results generally agree with the circular velocity estimates derived by Leung et al. (2018), Levy et al. (2018).

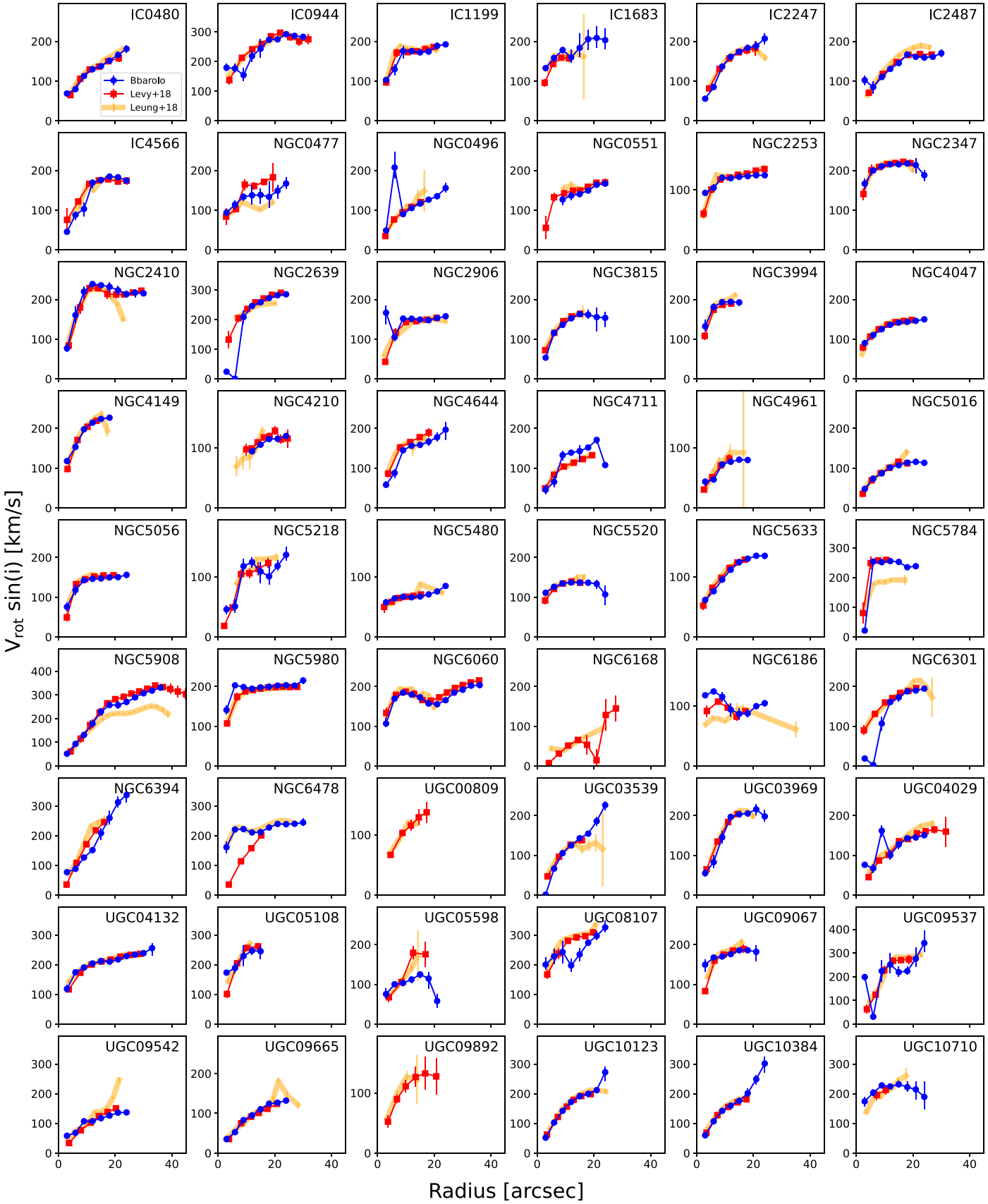

Figure 7. CO rotation curves derived from the `3D-Barolo` package (*blue circles*) compared to those previously published by Leung et al. (2018), Levy et al. (2018), for the sample of 54 galaxies studied by Leung et al. (2018). Circular velocities have been multiplied by a sin *i* factor to compensate for different adopted inclinations; the plotted curves should thus approximate the observed velocity widths. Differences are most apparent in the central rings, where varying treatment of beam smearing and velocity dispersion can have significant effects.

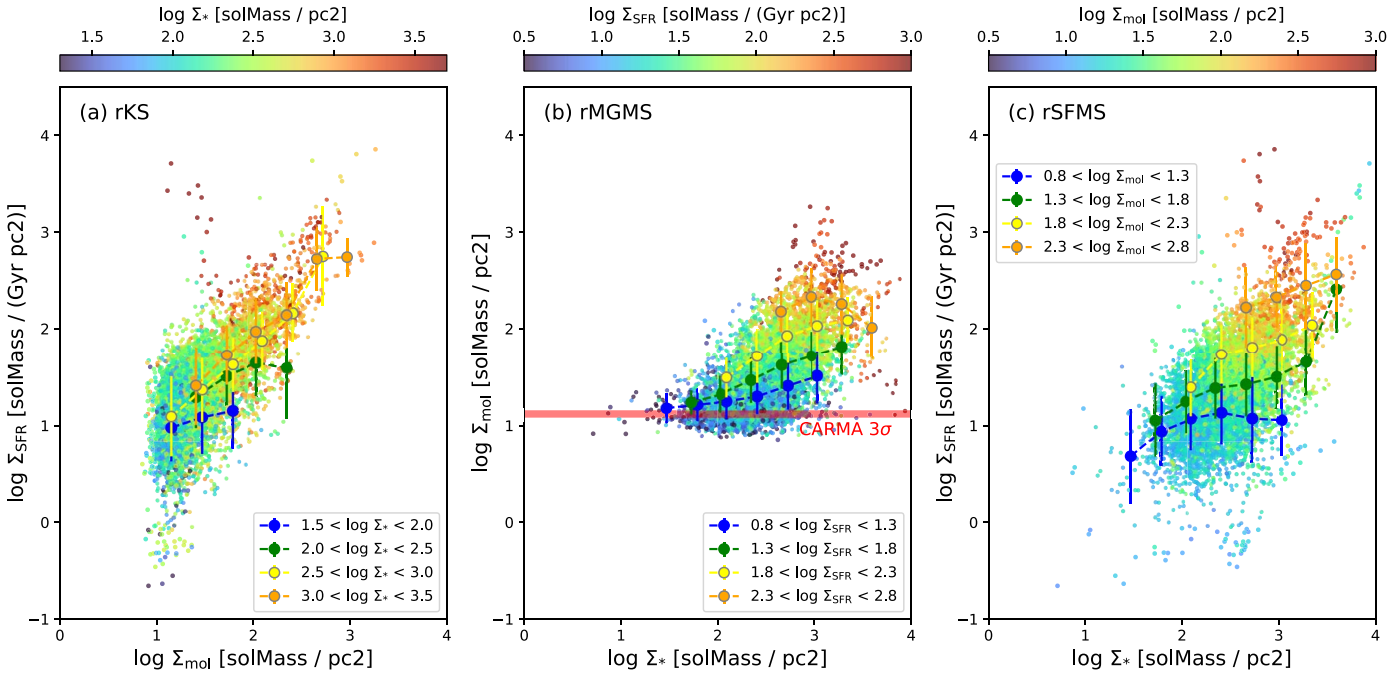

Figure 8. Mutual correlations between molecular gas surface density ($\Sigma_{\rm mol}$), star formation rate surface density (based on extinction-corrected Hα emission, $\Sigma_{\rm SFR}$), and stellar surface density (Σ_*) for the full set of square grid downsampled pixels. The three panels correspond to the Kennicutt–Schmidt, molecular gas main-sequence, and star-forming main-sequence diagrams respectively. Points in each panel are color coded and binned by the value of the third parameter. A horizontal line in the middle panel denotes the approximate sensitivity limit for the CARMA CO data.

3. Applications of the Database

3.1. Star Formation Scaling Relations

A straightforward application of the database is to make scatter plots comparing two flux-derived quantities. Recently, there has been much attention given to the relative tightness of observed relations between the stellar surface density Σ_*, the star formation surface density $\Sigma_{\rm SFR}$, and the molecular gas density $\Sigma_{\rm mol}$ (e.g., Lin et al. 2019; Sánchez et al. 2021). Figure 8 shows the mutual correlations between these three variables in EDGE. In each subpanel, the scatter points are colored and vertically binned by the value of the third variable. While each pair of variables is well correlated, the correlation between $\Sigma_{\rm SFR}$ and $\Sigma_{\rm mol}$, i.e., the resolved Kennicutt–Schmidt relation (rKS; Kennicutt 1998), appears to be the tightest and most independent of the third variable, as evidenced by the vertical color gradient in panels (b) and (c) of Figure 8. The resolved molecular gas main sequence (rMGMS; Lin et al. 2019) and resolved star-forming main sequence (rSFMS; Cano-Díaz et al. 2016) show a much clearer dependence on the third variable. This result is in agreement with studies based on the ALMaQUEST survey that have found the $\Sigma_{\rm SFR}$–$\Sigma_{\rm mol}$ relation to be the strongest among the three relations (Lin et al. 2019; Ellison et al. 2020; Baker et al. 2022).

Figure 9 provides a more quantitative characterization of the three relations, making use of the LEO-Py code (Feldmann 2019) to deduce the best-fit power-law relations taking into account censoring due to nondetections. Only the points from Figure 8 that are classified as star-forming (SF_BPT = 1) are used in the analysis. LEO-Py derives the fit parameters using likelihood maximization while assuming that the errors in both axes are uncorrelated, and each follows a normal distribution. The nondetections are provided as 3σ upper limits. The best-fit slope, intercept, and vertical scatter are included in the legend of each subpanel. The slopes of the three relations range from 0.8 to 1, thus being close to or slightly sublinear. For comparison, the results of an ordinary least-squares (OLS) fit to the detections only are shown as a dashed magenta line. The LEO-Py and OLS fits are most discrepant in panel (b), where the large number of CO nondetections leads to a bias toward high values of $\Sigma_{\rm mol}$ at low Σ_* and a resultant flattening of the OLS slope. This is less of an issue in panel (a) because the distribution of $\Sigma_{\rm SFR}$ values at a given $\Sigma_{\rm mol}$ is generally well-sampled and not strongly biased by nondetections.

Figure 10 summarizes the tightness of the three relations by comparing the Spearman partial correlation coefficients between each pair of variables. For each pair of variables X and Y, the partial correlation is the correlation between the residuals θ_X and θ_Y after removing the best-fit power laws relating X with Z and Y with Z respectively. It therefore signifies how well X and Y are expected to be correlated when Z is held constant. The partial correlation coefficients confirm that the rKS relation is the tightest correlation between any pair of variables. Although less tight than the rKS relation, the rMGMS shows a notably stronger partial correlation compared to the rSFMS, in agreement with the conclusion by Lin et al. (2019) from the ALMaQUEST survey that the rSFMS is largely a consequence of the other two relations. On the other hand, we find that the partial correlation coefficient between $\Sigma_{\rm SFR}$ and Σ_* is still positive, whereas Baker et al. (2022) find a value consistent with zero for the ALMaQUEST sample, which includes a substantial fraction (∼50%) of galaxies below the main sequence. Whether the sample selection effects, in particular the bias toward higher SFRs in EDGE, are responsible for this difference will be an important avenue for future investigation, since it has implications for whether

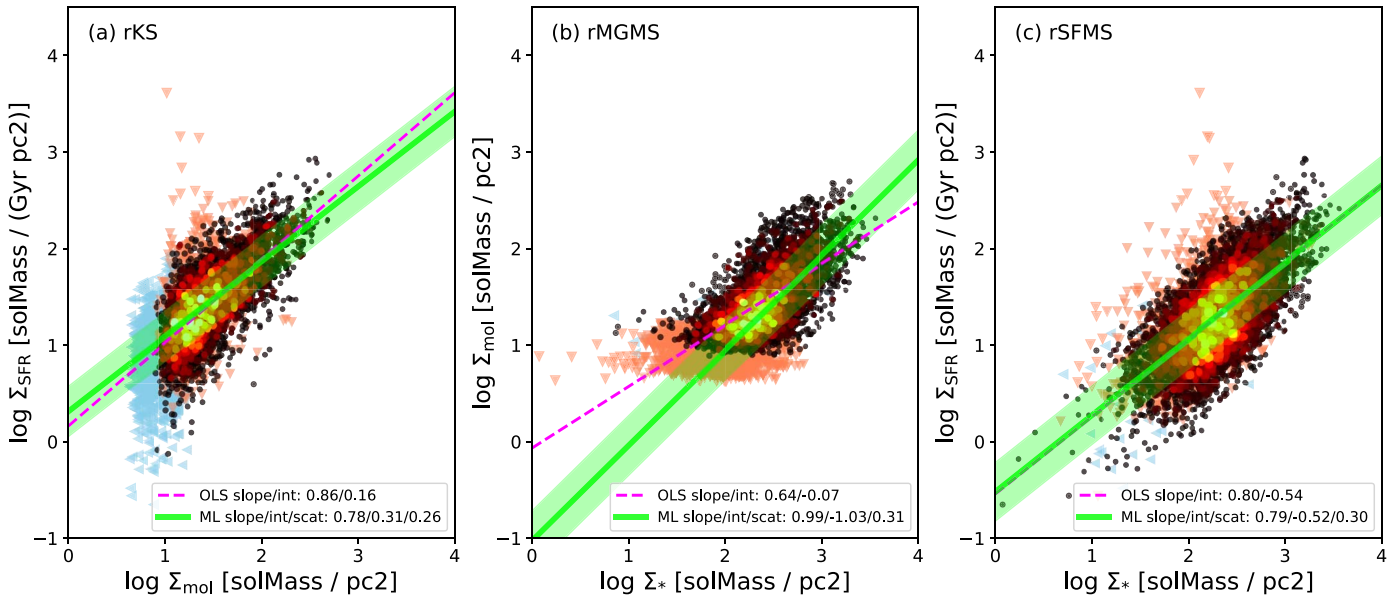

Figure 9. Same panels and data as in Figure 8, but limited to pixels classified as star-forming [below the Kauffmann et al. 2003 BPT curve and with EW(Hα) > 6 Å]. Upper limits are shown as pink triangles for the vertical axis and blue triangles for the horizontal axis. Overlaid are best-fit power-law relations based on ordinary least-squares (magenta dotted line) and LEO-Py, which takes into account nondetections (green solid line with vertical scatter indicated by shading).

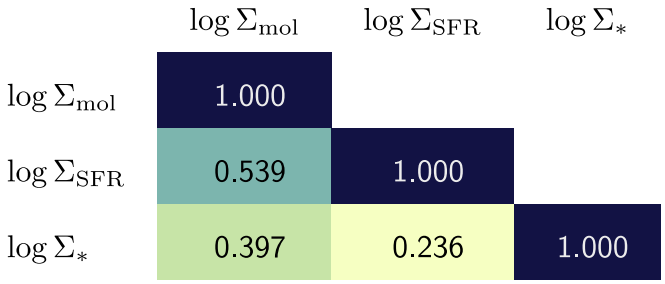

Figure 10. Spearman partial correlation coefficients calculated based on the LEO-Py fits. The coefficients indicate that the relation between $\Sigma_{\rm SFR}$ and $\Sigma_{\rm mol}$ is the tightest among the three correlation pairs.

Σ_* serves as an important secondary variable in the star formation law (e.g., Shi et al. 2018).

3.2. Spatially Resolved Star Formation Histories

Pipe3D models the stellar light as a linear combination of simple stellar populations taken from the GSD156 library (Cid Fernandes et al. 2013), which comprises 156 templates for 39 stellar ages (ranging from 1 Myr to 14.1 Gyr) and four metallicities ($Z/Z_\odot = 0.2$, 0.4, 1, and 1.5). For each spaxel, the light fraction contributed by each template is recorded in the `SFH` table. In order to reconstruct the star formation history, we scale the light fraction by each template's mass-to-light ratio, based on a Salpeter (1955) IMF, then multiply the derived mass fraction (summed over metallicity) by the total stellar mass in the spaxel. We display cumulative star formation histories for two EDGE galaxies, NGC 3687 (which has the prominent Hα ring shown in Figure 4), and NGC 5614 (an interacting galaxy in the Arp 178 triplet) in Figure 11, along with the corresponding radial profiles of specific SFR ($\rm sSFR = \Sigma_{SFR}/\Sigma_*$) based on extinction-corrected Hα emission. Despite the assumptions involved in recovering the SFH, the radial age trends implied by the SFH profiles are in qualitative agreement with the sSFR profiles, which show high sSFR values (indicative of a recent buildup of stellar mass) at large radii in NGC 3687 and at small radii in NGC 5614. We note that the ionized gas kinematics in NGC 5614 are highly disturbed (Barrera-Ballesteros et al. 2015), consistent with a recent inflow of gas toward the central regions that was triggered by the interaction.

4. Comparison of Python and SQL Databases

As discussed in Section 1, a previous implementation of the EDGE database using the SQLite language was used for results presented in Bolatto et al. (2017), Dey et al. (2019). In Figure 12, we compare the results obtained by Dey et al. (2019), studying the variables that most influence the spatially resolved SFR, with a reanalysis conducted using `edge_pydb`. Displayed is the standardized slope, which represents the coefficient (slope) of the multilinear fit for a given variable, scaled by its standard deviation to compensate for the fact that the variables spanning larger dynamic range can still exert a strong influence even with a relatively shallow power-law dependence. As expected, Σ_* and $\Sigma_{\rm mol}$ remain the most important factors determining $\Sigma_{\rm SFR}$, consistent with the results of Dey et al. (2019). The greater importance of Σ_* compared to $\Sigma_{\rm mol}$ may come as a surprise given the relative tightness of the resolved Kennicutt–Schmidt relation discussed in Section 3.1, but note that the limited dynamic range of the CO observations results in the $\Sigma_{\rm SFR}$–Σ_* relation spanning a greater logarithmic range in terms of significant detections (see Figure 9). Analyses such as those in Figure 12 that do not take the distribution of nondetections into account will therefore favor the quantities with a larger dynamic range as explanatory variables.

On the other hand, many of the quantities derived from the stellar analysis (metallicity Z_*, age τ_*, extinction A_V) show noticeably different standardized slopes compared to the previous work. An important distinction is that the SQL database was derived from a Pipe3D analysis of the native-resolution data cubes from CALIFA. Smoothing to match the CARMA resolution occurred *after* the extraction of the stellar population properties. On the other hand, for `edge_pydb`, we have degraded the spatial resolution of the CALIFA data to 7″

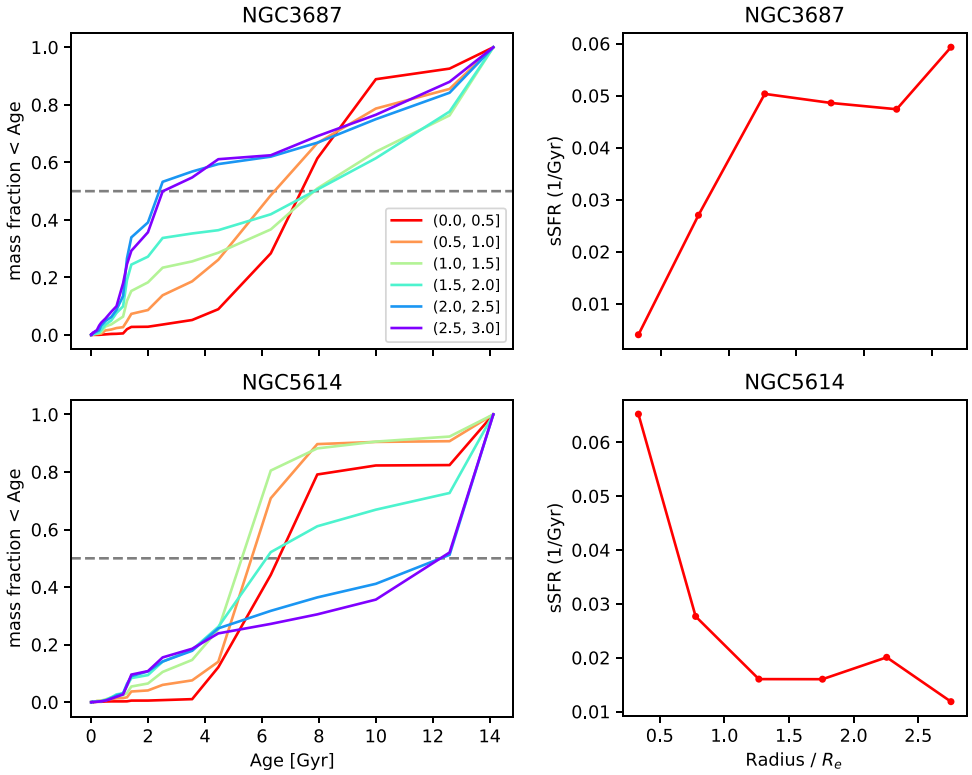

Figure 11. Cumulative star formation history, binned in radial rings from 0 to 3 R_e, for NGC 3687 (upper left, also shown in Figure 4) and NGC 5614 (lower left). The intersection of each curve with the dashed line indicates the median age at each radius. A relatively young age for the outskirts of NGC 3687 is inferred, whereas the inner regions appear younger in NGC 5614. These general trends are corroborated by the radial profiles of specific SFR ($\Sigma_{\rm SFR}/\Sigma_*$) shown in the right panels.

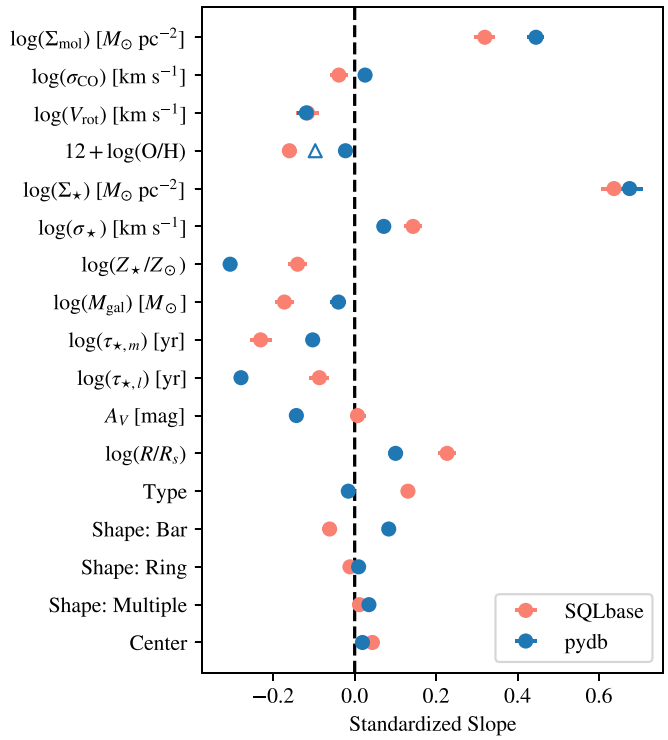

Figure 12. Comparison of SQL and `edge_pydb` databases, following the analysis of Dey et al. (2019). The "standardized slope" on the horizontal axis is the coefficient of each quantity considered in the multilinear fit for $\log\Sigma_{\rm SFR}$, scaled by the standard deviation of the same quantity in order to reflect its contribution to the fit. In both analyses, Σ_* and $\Sigma_{\rm mol}$ are the dominant contributors to the SFR. The blue open triangle for O/H shows the `edge_pydb` result if the N2 estimator used in the SQL database were to be used.

before running Pipe3D. In particular, the age and extinction are likely to vary spatially on scales comparable to the native CALIFA resolution of 2.″5 (∼1 kpc), so smoothing an age or extinction map may yield different results compared with sampling a map of the same quantity derived from a smoothed IFU cube. For both databases, the gas metallicity is derived from smoothed emission-line fluxes, so better consistency would be expected; however, Dey et al. (2019) use the N2 estimator for 12 + log(O/H) (Marino et al. 2013) whereas the present database employs the O3N2 estimator. The open triangle in Figure 12 shows the `edge_pydb` result if one applies the N2 estimator, which is more consistent with the earlier results. Furthermore, the additional smoothing when calculating the Balmer decrement described in Section 2.6.1 was not used in the SQL database; this has the potential to introduce additional shifts in all of the relations involving $\Sigma_{\rm SFR}$.

5. Summary and Future Work

In this paper, we have presented our basic approach to compiling a database of galaxy properties derived from spatially resolved CO and IFU observations. A strong emphasis on usability is essential to our approach, as the database is produced in order to conduct the science rather than as a benefit to the community after the science has been conducted. We take advantage of self-documenting formats now provided by Astropy tables, and provide sample notebooks that demonstrate how scientifically interesting plots can be generated from the data.

While the EDGE-CALIFA project began with a CALIFA subsample observed with CARMA, it has expanded as additional time has been secured to observe CALIFA galaxies

in CO with other millimeter facilities, including APEX (see Colombo et al. 2020), ACA (see Villanueva et al. 2024), the Large Millimeter Telescope, and GBT. The vast majority of CALIFA galaxies still lack spatially resolved CO observations, so the database will continue to grow over time. In addition, spatially resolved H I observations have recently been obtained for CALIFA galaxies using the Jansky Very Large Array and the Giant Metrewave Radio Telescope (PIs V. Kalinova & D. Colombo). The use of the `edge_carma` prefix in many of the HDF5 file names implicitly recognizes that the current database is tailored to the initial CARMA sample. Readers wishing to reproduce the exact results of this paper should access the appropriate version of the database as stored in the Github version history. The EDGE database architecture can easily be adapted to other IFU surveys, particularly when Pipe3D has been used for spectral fitting, and will continue to be updated as Pipe3D itself undergoes further development (e.g., Sánchez et al. 2023).

The current version of `edge_pydb` at the time of this publication is indexed on Zenodo doi:10.5281/zenodo.10431797. The full-pixel tables are also available to download from Zenodo doi:10.5281/zenodo.10256731.

Acknowledgments

We thank the anonymous referee for helpful suggestions, which substantially improved this paper. This work was funded in part by NSF AAG grants 1616199 and 2307440 to the University of Illinois, 1615960 and 2307441 to the University of Maryland, and 1616924 to the University of California-Berkeley. R.C.L. acknowledges partial support from a NSF Astronomy and Astrophysics Postdoctoral Fellowship under award AST-2102625. M.R. wishes to acknowledge partial support from ANID Basal FB210003. V.V. acknowledges support from the scholarship ANID-FULBRIGHT BIO 2016-56160020 and funding from NRAO Student Observing Support SOSPADA-015. J.B.-B. acknowledges support from the grant IA-101522 (DGAPA-PAPIIT, UNAM) and funding from the CONACYT grant CF19-39578. Support for CARMA construction was derived from the Gordon and Betty Moore Foundation, the Kenneth T. and Eileen L. Norris Foundation, the James S. McDonnell Foundation, the Associates of the California Institute of Technology, the University of Chicago, the states of California, Illinois, and Maryland, and the NSF. CARMA development and operations were supported by the NSF under a cooperative agreement and by the CARMA partner universities. This research is based on observations collected at the Centro Astronómico Hispano-Alemán (CAHA) at Calar Alto, operated jointly by the Max-Planck Institut für Astronomie (MPA) and the Instituto de Astrofisica de Andalucia (CSIC). This research has made use of NASA's Astrophysics Data System. This publication makes use of data products from the Wide-field Infrared Survey Explorer, which is a joint project of the University of California, Los Angeles, and the Jet Propulsion Laboratory/California Institute of Technology, funded by the National Aeronautics and Space Administration.

Software: Astropy (Astropy Collaboration et al. 2013, 2018, 2022), `3D-Barolo` (Di Teodoro & Fraternali 2015), `LEO-Py` (Feldmann 2019).

ORCID iDs

Tony Wong https://orcid.org/0000-0002-7759-0585
Yixian Cao https://orcid.org/0000-0001-5301-1326
Yufeng Luo https://orcid.org/0000-0002-4623-0683
Alberto D. Bolatto https://orcid.org/0000-0002-5480-5686
Sebastián F. Sánchez https://orcid.org/0000-0001-6444-9307
Jorge K. Barrera-Ballesteros https://orcid.org/0000-0003-2405-7258
Leo Blitz https://orcid.org/0000-0002-4272-4432
Helmut Dannerbauer https://orcid.org/0000-0001-7147-3575
Adam K. Leroy https://orcid.org/0000-0002-2545-1700
Rebecca C. Levy https://orcid.org/0000-0003-2508-2586
Xincheng Lin https://orcid.org/0000-0001-9068-6787
Yuanze Luo https://orcid.org/0000-0002-0696-6952
Erik W. Rosolowsky https://orcid.org/0000-0002-5204-2259
Mónica Rubio https://orcid.org/0000-0002-5307-5941
Peter Teuben https://orcid.org/0000-0003-1774-3436
Dyas Utomo https://orcid.org/0000-0003-4161-2639
Vicente Villanueva https://orcid.org/0000-0002-5877-379X
Stuart N. Vogel https://orcid.org/0000-0002-8765-7915

References

Abazajian, K. N., Adelman-McCarthy, J. K., Agüeros, M. A., et al. 2009, ApJS, 182, 543
Accurso, G., Saintonge, A., Catinella, B., et al. 2017, MNRAS, 470, 4750
Alloin, D., Collin-Souffrin, S., Joly, M., & Vigroux, L. 1979, A&A, 78, 200
Astropy Collaboration, Price-Whelan, A. M., Lim, P. L., et al. 2022, ApJ, 935, 167
Astropy Collaboration, Price-Whelan, A. M., Sipőcz, B. M., et al. 2018, AJ, 156, 123
Astropy Collaboration, Robitaille, T. P., Tollerud, E. J., et al. 2013, A&A, 558, A33
Baker, W. M., Maiolino, R., Bluck, A. F. L., et al. 2022, MNRAS, 510, 3622
Baldwin, J. A., Phillips, M. M., & Terlevich, R. 1981, PASP, 93, 5
Barrera-Ballesteros, J. K., García-Lorenzo, B., Falcón-Barroso, J., et al. 2015, A&A, 582, A21
Barrera-Ballesteros, J. K., Heckman, T., Sánchez, S. F., et al. 2018, ApJ, 852, 74
Barrera-Ballesteros, J. K., Sánchez, S. F., Heckman, T., et al. 2021, MNRAS, 503, 3643
Belfiore, F., Maiolino, R., Maraston, C., et al. 2016, MNRAS, 461, 3111
Bigiel, F., Leroy, A., Walter, F., et al. 2008, AJ, 136, 2846
Bitsakis, T., Sánchez, S. F., Ciesla, L., et al. 2019, MNRAS, 483, 370
Bolatto, A. D., Wolfire, M., & Leroy, A. K. 2013, ARA&A, 51, 207
Bolatto, A. D., Wong, T., Utomo, D., et al. 2017, ApJ, 846, 159
Bottinelli, L., Gouguenheim, L., Paturel, G., & de Vaucouleurs, G. 1983, A&A, 118, 4
Brinchmann, J., Charlot, S., White, S. D. M., et al. 2004, MNRAS, 351, 1151
Calzetti, D., Wu, S. Y., Hong, S., et al. 2010, ApJ, 714, 1256
Cano-Díaz, M., Sánchez, S. F., Zibetti, S., et al. 2016, ApJL, 821, L26
Cao, Y., Wong, T., Bolatto, A. D., et al. 2023, ApJS, 268, 3
Cardelli, J. A., Clayton, G. C., & Mathis, J. S. 1989, ApJ, 345, 245
Catalán-Torrecilla, C., Gil de Paz, A., Castillo-Morales, A., et al. 2015, A&A, 584, A87
Chiang, I. D., Sandstrom, K. M., Chastenet, J., et al. 2024, ApJ, in press (arXiv:2311.00407)
Cid Fernandes, R., Pérez, E., García Benito, R., et al. 2013, A&A, 557, A86
Cid Fernandes, R., Stasińska, G., Schlickmann, M. S., et al. 2010, MNRAS, 403, 1036
Colombo, D., Kalinova, V., Utomo, D., et al. 2018, MNRAS, 475, 1791
Colombo, D., Sanchez, S. F., Bolatto, A. D., et al. 2020, A&A, 644, A97
Dey, B., Rosolowsky, E., Cao, Y., et al. 2019, MNRAS, 488, 1926
Di Teodoro, E. M., & Fraternali, F. 2015, MNRAS, 451, 3021
Ellison, S. L., Thorp, M. D., Lin, L., et al. 2020, MNRAS, 493, L39
Ellison, S. L., Wong, T., Sánchez, S. F., et al. 2021, MNRAS, 505, L46
Feldmann, R. 2019, A&C, 29, 100331

Garay-Solis, Y., Barrera-Ballesteros, J. K., Colombo, D., et al. 2023, ApJ, 952, 122
González Delgado, R. M., Cid Fernandes, R., Pérez, E., et al. 2016, A&A, 590, A44
Kauffmann, G., Heckman, T. M., Tremonti, C., et al. 2003, MNRAS, 346, 1055
Kennicutt, R. C., & Evans, N. J. 2012, ARA&A, 50, 531
Kennicutt, R. C., Jr. 1998, ApJ, 498, 541
Kewley, L. J., Dopita, M. A., Sutherland, R. S., Heisler, C. A., & Trevena, J. 2001, ApJ, 556, 121
Kroupa, P., Tout, C. A., & Gilmore, G. 1993, MNRAS, 262, 545
Leung, G. Y. C., Leaman, R., van de Ven, G., et al. 2018, MNRAS, 477, 254
Levy, R. C., Bolatto, A. D., Sánchez, S. F., et al. 2019, ApJ, 882, 84
Levy, R. C., Bolatto, A. D., Teuben, P., et al. 2018, ApJ, 860, 92
Lin, L., Pan, H. A., Ellison, S. L., et al. 2019, ApJL, 884, L33
Makarov, D., Prugniel, P., Terekhova, N., Courtois, H., & Vauglin, I. 2014, A&A, 570, A13
Marino, R. A., Rosales-Ortega, F. F., Sánchez, S. F., et al. 2013, A&A, 559, A114
Masters, K. L., Crook, A., Hong, T., et al. 2014, MNRAS, 443, 1044
Pettini, M., & Pagel, B. E. J. 2004, MNRAS, 348, L59
Saintonge, A., & Catinella, B. 2022, ARA&A, 60, 319
Saintonge, A., Catinella, B., Tacconi, L. J., et al. 2017, ApJS, 233, 22
Saintonge, A., Kauffmann, G., Wang, J., et al. 2011, MNRAS, 415, 61
Salim, S., Rich, R. M., Charlot, S., et al. 2007, ApJS, 173, 267
Salpeter, E. E. 1955, ApJ, 121, 161
Sánchez, S. F., Barrera-Ballesteros, J. K., Colombo, D., et al. 2021, MNRAS, 503, 1615
Sánchez, S. F., Galbany, L., Walcher, C. J., García-Benito, R., & Barrera-Ballesteros, J. K. 2023, MNRAS, 526, 5555
Sánchez, S. F., García-Benito, R., Zibetti, S., et al. 2016a, A&A, 594, A36
Sánchez, S. F., Kennicutt, R. C., Gil de Paz, A., et al. 2012, A&A, 538, A8
Sánchez, S. F., Pérez, E., Sánchez-Blázquez, P., et al. 2016b, RMxAA, 52, 171
Schlegel, D. J., Finkbeiner, D. P., & Davis, M. 1998, ApJ, 500, 525
Shi, Y., Yan, L., Armus, L., et al. 2018, ApJ, 853, 149
Springob, C. M., Haynes, M. P., Giovanelli, R., & Kent, B. R. 2005, ApJS, 160, 149
Utomo, D., Bolatto, A. D., Wong, T., et al. 2017, ApJ, 849, 26
van Driel, W., Marcum, P., Gallagher, J. S., et al. 2001, A&A, 378, 370
Villanueva, V., Bolatto, A., Vogel, S., et al. 2021, ApJ, 923, 60
Villanueva, V., Bolatto, A. D., Vogel, S. N., et al. 2024, ApJ, 962, 88
Wong, T., & Blitz, L. 2002, ApJ, 569, 157
Wong, T., Xue, R., Bolatto, A. D., et al. 2013, ApJL, 777, L4
Wright, E. L., Eisenhardt, P. R. M., Mainzer, A. K., et al. 2010, AJ, 140, 1868